Article

Comprehensive Analysis of BDS/GNSS Differential Code Bias and Compatibility Performance

Yafeng Wang [1,2,3], Dongjie Yue [1,*], Hu Wang [2,3,4], Hongyang Ma [5], Zhiqiang Liu [1] and Caiya Yue [4,6]

1   School of Earth Sciences and Engineering, Hohai University, Nanjing 211100, China; wyf_gnss@hhu.edu.cn (Y.W.); zhiqiangliu@hhu.edu.cn (Z.L.)
2   Chinese Academy of Surveying and Mapping, Beijing 100036, China; wanghu@casm.ac.cn
3   Key Laboratory of Surveying and Mapping Science and Geospatial Information Technology of MNR, CASM, Beijing 100036, China
4   Beijing Fangshan Human Satellite Laser National Field Scientific Observation and Research Station, Beijing 100036, China; yuecaiya@lcu.edu.cn
5   School of Geomatics Science and Technology, Nanjing Tech University, Nanjing 210037, China; mahongyang@njtech.edu.cn
6   School of Geography and Environment, Liaocheng University, Liaocheng 252059, China
*   Correspondence: yuedongjie@hhu.edu.cn

Abstract: High-precision DCBs are essential for effective multi-frequency and multi-constellation GNSS integration, especially in processing compatible signal observations. This study utilizes data from MGEX, iGMAS, and CORS stations to estimate and analyze long time series of BDS/GNSS DCBs, focusing on stability and influencing factors. Results indicate that DCBs for the same signal, but different channels exhibit similar ranges and trends. Among BDS DCBs, those from satellites with rubidium atomic clocks are more stable than those with hydrogen atomic clocks. An upgrade and maintenance of BDS in late 2022, reported by NABU, likely contributed to DCB jumps. BDS-compatible signal DCBs show weaker stability compared to GPS and Galileo. Variations in GNSS signal processing and receiver algorithms also impact DCB stability. Converting DCBs to OSBs and performing RMS statistics revealed that smaller differences between signals increase the susceptibility of observation equations to observation quality.

Keywords: differential code bias; BDS-3; compatibility; observable-specific signal bias

1. Introduction

GNSS technology has advanced significantly in recent years. GPS and GLONASS have reached the generation upgrade development stage; meanwhile, the construction of BDS constellation has been completed. The 57th and 58th BDS MEO satellites were launched into orbit on 26 December 2023. Galileo will complete the full deployment of the first generation system in 2025. In addition, the rapid construction of MGEX also provides support for GNSS development. Multi-frequency and multi-channel signals provide rich observational data for satellite applications while also bringing new challenges.

DCB (differential code bias) is defined as the time delay between two or more types of GNSS signals. It is further classified into satellite DCB and receiver DCB based on the corresponding hardware components. In addition, intra-frequency and inter-frequency biases are defined according to whether the frequencies are the same or not [1,2]. The total ionosphere electron content is greatly influenced by the accuracy of DCB, which is a crucial error that must be separated for ionosphere modeling and can result in a bias of around 30 TECU (total electron content unit) [3], affecting the accuracy of navigation and positioning [4,5].

DCB can be estimated by two methods: one is estimating the DCB simultaneously during ionosphere modeling [6], and the other is using an external ionosphere product as

a constraint [7], e.g., an empirical ionosphere model or an ionosphere product [8,9]. The geometry-free linear combination of phase-smoothed range (GFPSR) method [10] is widely used to extract ionosphere delays and DCB parameters, but this method is affected by observation length and multipath [11]. Therefore, some scholars propose using the PPP (precise point positioning) [12,13] algorithm for estimating DCB. Liu et al. [14] estimated triple-frequency DCB by using the UPPP (uncombined precise point positioning) method and demonstrated that the algorithm has higher accuracy compared with those from the traditional dual-frequency carrier-to-code level (CCL) method, but it still relies on the existing clock products in the uncombined process. When extracting ionosphere delays, Shi et al. [15] combined uncombined and GF (geometry-free) algorithms, calculated the weight matrix by using the weighted least-squares adjustment to obtain the multi-frequency multi-system DCB. Since this method does not rely on existing ionosphere products, the issue of missing orbits and clock products would be avoided. On the basis of these studies, Fan et al. [16] established a general model with GFPSR and triple-frequency UPPP and then derived an equation for the triple-frequency DCB. The results showed that the estimated DCB from this model was more stable, in which the average value of the BDS DCBs improved by more than 20% compared to the conventional GFPSR model. However, this method is only applicable regionally.

The satellite DCB is relatively stable, while the receiver DCB (RDCB) may significantly change over the course of hours or minutes, affected by the ambient temperature, receiver type, antenna type, cable brand, etc. RDCB has become one of the important factors affecting ionosphere TEC extraction due to the unclear variation characteristics and the limited estimation methods. Liu et al. [17] studied the association between receiver type, antenna type, ambient temperature, Doppler effect, and receiver DCB by estimating RDCB over a short period of time using MCCL (Modified Carrier-to-code Leveling) method. The result showed that the stability of RDCB can vary between different receiver types from different manufacturers, and the receiver antenna has less influence on the stability of RDCB. In addition, there is a strong correlation between receiver DCB and Doppler shift, and the correlation coefficient for some satellites can reach 90%. However, most of the above studies focus on the changes in the receiver DCB within days or months, and the analysis of the receiver DCB long time series is relatively rare.

By the end of 2022, GPS already broadcast signals at L1C (1575.42 MHz), L2C (1227.60 MHz), and L5C (1176.45 MHz); GLONASS broadcast signals at G1 ($1602 + k \times 9/16$, k= $-7 \dots +12$), G2 ($1246 + k \times 7/16$), and G3 (1202.025 MHz); Galileo broadcast signals at E1 (1575.42 MHz), E5a (1176.45 MHz), E5b (1207.140 MHz), E6 (1278.75 MHz), and E5(a + b) (1191.795 MHz); BDS broadcast signals at B1C (1575.42 MHz), B1I (1561.098 MHz), B2a (1176.45 MHz), B2b (1207.140 MHz), B3I (1268.52 MHz), and B2 (B2a + B2b) (1191.795 MHz) [18]. The GPS, GLONASS, and Galileo constellations are composed of MEO satellites, while BDS has three types of orbiting satellites, including MEO, IGSO and GEO satellites. Many scholars have conducted a series of studies on the multi-frequency and multi-system DCB. Yasyukevich et al. [19] studied the effect of GPS and GLONASS DCB on TEC and discovered that in some instances, the effect displays seasonal variations with an amplitude of up to 20 TECU. Mylnikova et al. [20] found that there is systematic variability of TEC estimation errors associated with DCBs, with 1 TECU/year for GPS and three times (3 TECU/year) for GLONASS. Li et al. [21] found the high stability of Galileo DCBs by analyzing the three-year data. Montenbruck et al. [22] found that the two frequencies E5a/E5b are well matched in both combined and individual cases with very little distinction in their correspondent DCB, which represents a good quality of signal generation and transmission of E5(a + b) despite the extremely high bandwidth. Shi [23] performed a multipath analysis of the new signals in BDS-3, which showed that B1C frequency has the worst signal quality and B2 (a + b) frequency has the best. Mi et al. [24] found that the difference between BDS-2 and BDS-3 B1I-B3I DCB can cause an error up to 1.128 m. In this case, such difference must be considered to eliminate the possible negative effects on PNT (positing, navigating, timing) applications. Zheng et al. [25] also considered the overlapping signals of BDS-2

and BDS-3 when conducting global ionospheric modeling and DCB estimation, solving BDS-2 and BDS-3 DCB as two sets of unknown parameters. The results showed that the difference between BDS-2 and BDS-3 DCB could reach 8 ns, indicating that this difference cannot be ignored in DCB estimation. Jin et al. [26] evaluated the BDS DCBs and showed that the GEO satellites have worse DCB stability than other types of satellites due to the relatively large noise of the GEO satellites related to the ionosphere observation error. In summary, as a by-product of ionosphere, the accuracy of DCB is not only affected by different ionosphere models, equivalent heights, projection functions, interpolation fits algorithm, etc., but also by the variation in ionosphere TEC due to solar activity, geomagnetic activity, weather environment, etc. Wijaya et al. [27] achieved fast estimation of GPS DCB using an orthogonal transformation method and process matrix decomposition. However, this method is limited to local stations and is not applicable globally. Wang et al. [28] directly estimated VTEC in the observation equation and independently estimated DCB. This method has good accuracy in estimating TEC and DCB under low solar activity, but during periods of high solar activity, the algorithm tends to remove many observations, leading to poorer estimation results. Wang [29] also estimated the DCB of multiple systems, finding that the DCB results of GPS and Galileo compatible frequencies were larger than those of other frequencies, and the RMS of the X channel was smaller than that of the Q channel, attributing this to limited observation data. Yuan et al. [30] analyzed the DCB stability of BDS-3 satellites and found that the stability of IGSO satellites was higher than that of MEO satellites. However, the author did not provide a specific analysis. For some satellites (such as C28) with poor monthly stability, the author attributed this mainly to the satellites' health status during the month. Most of the studies mentioned above focus on the estimation of DCB for a single system or a specific frequency combination, with a notable lack of comprehensive and in-depth research on multi-frequency and multi-system DCB joint estimation.

Scholars have investigated the extended-term performance of DCB. Liu et al. [31] employed professional calibration equipment to simulate GPS navigation hardware signals and assessed the temporal variation in DCB through hardware calibration. The findings reveal a gradual increase in DCB by 0.627 ns over approximately 41.5 months, with a monthly increment of 0.0151 ns, demonstrating consistent changes in the receiver DCB. In their analysis of DCB values for GPS satellites spanning from 2000 to 2019, Xiang et al. [32] identified six influencing factors on satellite DCB: changes in the zero-mean datum constraint, satellite vehicles, NANU (Notice Advisory to Navstar Users) messages, Flex power, solar activity, and satellite PRNs and types. Bao et al. [33] conducted an analysis of factors influencing BDS DCB based on a three-month dataset, uncovering correlations between BDS DCB changes, frequency, and satellite orbit. Additionally, the stability of MEO and IGSO DCB is linked to the satellite's repeated orbit cycle, leading to observation errors attributed to multipath effects. In their comparative study of products released by CAS (Chinese Academy of Sciences) and DLR (Deutsches Zentrum für Luft- und Raumfahrt) in 2021, Cui [34] discovered semi-annual or periodic terms in C1W-C2W DCB for some satellites, primarily attributable to residual ionospheric effects. Furthermore, a distinct linear trend in GPS satellite DCB is observed, primarily associated with the adopted zero baseline constraint. The above studies predominantly concentrate on investigating GPS satellite DCB, with BDS primarily addressing BDS-2 and limited exploration of BDS-3. Given the successful networking of BDS-3 in June 2020 and its stability over approximately three years, there is a scarcity of research on the long-term analysis of BDS-3 satellite DCB. By comparing and analyzing the long-term trends and characteristics of BDS-3/GNSS DCB, one can identify the compatibility and differences between systems. This provides a crucial basis for developing multi-system fusion strategies and interoperability specifications.

Most of the ionosphere analysis centers provide GPS DCB in the ionosphere file, and currently, only DLR and CAS can continuously provide multi-frequency and multi-system DCB products. In addition, DLR products have only been updated to the year 2021. These two analysis centers do not provide all types of DCB, and the quantity of receiver DCB

is influenced by the station selection strategy [35]. Therefore, users may not have the required station DCB or still need to linearly combine the existing DCB products, which will reduce the accuracy of the DCB and affect the performance of the PNT. Therefore, we have added DCB product types to the existing DCB product types in our research and selected 364 stations, including IGS (International GNSS Service), MGEX (Multi-GNSS Experiment), iGMAS (international GNSS Monitoring and Assessment System) and some regional CORSs (Continuously Operating Reference Stations), which have greatly enriched the receiver DCB.

In the conventional method, steps such as frequency selection and combining are usually performed before estimating and correcting DCB. For simplicity, some scholars [36] proposed the estimation method of OSB oriented to the original observations and gave a method for conversion between DCB and OSB. OSB can effectively avoid the inconvenience caused by various frequency selections and combinations and can be directly applied as a correction to observations. The pseudorange OSB values obtained from DCB conversion do not represent the actual hardware delay biases in pseudorange observations; instead, they are a combined form of the true pseudorange hardware delays. The OSB provides users with a bias that can be directly applied to raw observations, facilitating effective evaluation and analysis of DCB's internal consistency. Additionally, OSB values indicate the magnitude of bias for specific frequencies and signal types, providing a more intuitive representation of the quality of different signal types. The IGS working group clearly defined the processing and file format of OSB in Bias SINEX 1.00. In the same year, the Radio Technical Commission for Maritime Service standard (RTCM) also introduced the use of OSB in State Space Representations (SSRs). Wang [37] conducted estimations of the OSB for both GPS and GLONASS. Their findings indicate that the stability of OSB is influenced by solar activity intensity. Additionally, the OSB of GLONASS is twice that of GPS, attributed to inter-frequency bias. Deng et al. [38] estimate the multi-system GNSS OSB, and the results show that GLONASS is affected by inter-frequency bias (IFB) and BDS is affected by inter-system bias (ISB), and the OSB accuracy of these two systems is lower than GPS and Galileo. O. Montenbruck [39] estimated the data and pilot biases in GNSS signals, determining both the biases between different signal channels and the bias ratios within the signals. Ke et al. [40] conducted an estimation and analysis of BDS pseudorange OSBs with high temporal resolution. Their results indicated that, in the absence of ionospheric combinations and geometric distance effects, the biases of C2I and C6I have the same sign, with the absolute value of C2I generally smaller than that of C6I. Additionally, Ke [41] estimated the OSBs for CDMA and FDMA models in GPS, GLONASS, Galileo, and BDS. The results showed that GPS has the highest OSB stability, while BDS exhibits the poorest stability, which is attributed to the pseudorange observation quality of BDS's GEO satellites. Therefore, a long-term comprehensive analysis of OSB characteristics across different systems and frequencies is beneficial for evaluating the stability of satellite navigation systems and for further enhancing the performance and reliability of GNSS positioning.

This study primarily analyzes the DCB results of the new BDS/GNSS signals over 31 months, discussing the characteristics of the DCB time series, including influencing factors and stability. Additionally, we estimate and evaluate the DCB of compatible signals for GPS, Galileo, and BDS satellites, examining the compatibility of satellite signals to provide a reference for multi-system integrated data processing. We also estimate the receiver DCB for compatible signals and analyze the possible factors affecting the receiver-compatible signal DCB. Finally, we convert the DCB to OSB and analyze various types of satellite observations in the form of OSB.

This paper is structured as follows: this section is the introduction. Section 2 presents the DCB estimation method, OSB calculation algorithm, and introduction to the GNSS signals. Section 3 introduces the long-term DCB analysis between BDS signals, followed by an analysis of satellite DCB compatibility. The performance of receiver DCBs is also analyzed, and the consistency of the results with existing products is verified by utilizing the OSB RMS. Section 4 presents the summary and conclusion.

2. Methods and Data

2.1. DCB Estimation Method

We utilized two types of pseudorange observations from the global multi-frequency multi-system GNSS receivers for estimating DCB. After neglecting the effects of pseudorange observation noise and multipath effects, the observation model [42] can be expressed as follows:

$$
\begin{cases}
P_{r,i}^s = \rho_r^s + c \cdot (dt_r - dt^s) + T_r^s + I_{r,i}^s - c \cdot B_{r,i} - c \cdot B_i^s \\
P_{r,j}^s = \rho_r^s + c \cdot (dt_r - dt^s) + T_r^s + I_{r,j}^s - c \cdot B_{r,j} - c \cdot B_j^s
\end{cases}
\tag{1}
$$

where $P_{r,i}^s$ and $P_{r,j}^s$ are pseudorange observations at frequency i and j; ρ_r^s denotes the geometric distance from the satellite to the receiver; c denotes the speed of light; dt_r and dt^s represent the clock errors of the receiver and the satellite; T_r^s denotes the tropospheric delay error; $I_{r,i}^s$ and $I_{r,j}^s$ denote the ionosphere delay error at frequency i and j; $B_{r,i}$ and B_i^s denote the hardware delay effects of the receiver and the satellite in the observations.

The above two pseudorange observations are combined by a geometry-free distance model to obtain a combined expression for ionosphere delay and DCB as follows:

$$
P_4 = P_{r,2}^s - P_{r,1}^s = I_{r,2}^s - I_{r,1}^s - c(DCB_r - DCB^s)
\tag{2}
$$

where $DCB_r = B_{r,i} - B_{r,j}$ and $DCB_r = B_i^s - B_j^s$ are the differential code biases at the receiver side and the satellite side. $I_{r,i}^s = 40.3 \cdot STEC / f_i^2$ and $I_{r,j}^s = 40.3 \cdot STEC / f_j^2$, where $STEC$ is defined as slant TEC (STEC).

When two frequencies are the same, i.e., $i = j$, only the DCB parameter remains on the right side of the equation, and we estimate the DCB as the intra-frequency bias. When the two frequencies are different, i.e., $i \neq j$, we need to eliminate the ionosphere parameter to estimate the DCB accurately, and we use the CODE global ionosphere map (GIM) products (www.aiub.unibe.ch/download/CODE/, accessed on 1 November 2024) as an external constraint to eliminate the ionosphere parameter. Then, we can obtain the integrated expression [43] of DCB_r, DCB^s as follows:

$$
\begin{cases}
c \cdot (DCB_r + DCB^s) = P_4 - \dfrac{40.3(f_1^2 - f_2^2)}{f_1^2 f_2^2} STEC \\
VTEC = STEC \cdot M(z)
\end{cases}
\tag{3}
$$

where $M(z)$ is a single layer mapping function [44].

$$
M(z) = \cos(\arcsin(\frac{R}{R + H} \sin(\alpha z)))
\tag{4}
$$

where R is the radius of the Earth; H is the assumed height of the single layer ionosphere model, usually taken as 350 km; $\alpha = 0.9782$; z is the altitude angle of the receiver.

After correcting the ionosphere parameters, the only unknown parameters in Equation (3) are the DCB_r and DCB^s. We usually treat the DCB of each satellite and receiver as constant within-day data processing, and the estimated results are averaged to avoid the effects of observation noise and multipath. Since the DCB_r and DCB^s are linearly correlated, the observation matrix is rank-deficient. We separated the DCB_r and DCB^s by using the zero-mean condition, which is that the sum of all satellite DCBs in a day is zero so as to satisfy the full rank condition.

2.2. Benchmark Uniformity

The DCB products estimated by various institutions may have different satellite numbers, and the disappearance or appearance of satellites can lead to benchmark changes. Therefore, when comparing DCB products from different institutions or between different days, it is essential to unify the benchmark to ensure stable analysis of the DCB.

Assuming that the benchmark *A* has *m* satellites and using satellites where the sum of all DCBs is zero, the constraint equations [45] are as follows:

$$\begin{cases} I_m \hat{X} = 0 \\ I_m = \begin{bmatrix} 1 & 1 & \cdots & 1 \end{bmatrix}_{1 \times m} \end{cases} \tag{5}$$

where I_m is the coefficient vector, $\hat{X}$ is the DCB parameters of satellites under the benchmark *A*; if it is converted to a new benchmark *B* (*n* satellites under the new benchmark *B*, $n < m$), *n* satellites need to be constrained with zero benchmark, and the equation is as follows:

$$\begin{cases} C_m \hat{X}' = 0 \\ C_m = [I_n, O_{m-n}]_{1 \times m} \\ O_{m-n} = \begin{bmatrix} 0 & 0 & \cdots & 0 \end{bmatrix}_{1 \times (m-n)} \end{cases} \tag{6}$$

where $\hat{X}'$ is the satellite DCB under the new benchmark *B*, C_m is the constraint vector, and the conversion formula of the parameters between different benchmarks can be expressed as

$$\hat{X}' = \left(I - C_m^T \left(C_m C_m^T \right)^{-1} C_m \right) \hat{X} \tag{7}$$

2.3. GNSS Signal Modulation

At the initial stage of satellite navigation system construction, frequency resources were relatively abundant. However, with the development of GNSS satellites, fewer navigation frequencies are available. Thus, the concept of GNSS compatibility was proposed by a report on the third meeting of the International Committee on Global Navigation Satellite Systems (ICG). Compatibility is defined as the use of multi-GNSS and augmentation systems separately or in combination, without causing unacceptable interference or harming the operation and services of other single satellite navigation systems. Interoperability, in contrast, entails considerations related to signals, system time, and geodetic reference frames [46]. To effectively address the challenges of interoperability and compatibility, numerous collaborative projects have been launched at both national and international levels [47].

GPS L1C, Galileo E1 and BDS B1C signals own the same frequency of 1575.42 MHz, and this frequency also overlaps with India's NAVIC (Navigation Indian Constellation) L1 and Japanese QZSS (Quasi-Zenith Satellite System) L1C signals. Moreover, the signals of GPS L5, Galileo E5a, and BDS B2a share the same frequency band, and they overlap with signals from Indian NAVIC L5 and Japanese QZSS. Among these signals, the first category uses the Multiplexed Binary Offset Carrier (MBOC (6, 1, 1/11)) method, and the second category uses the Binary Phase Shift Keying (BPSK) method. The choice of modulation scheme significantly impacts compatibility. A key priority for future GNSS systems [48] is the adoption of modulation schemes with constant envelope and continuous phase. Except for the different modulation methods, the frequency, bandwidth, and code rate of GNSS signals also influence system compatibility and anti-interference capability. Previous studies have shown that combining main lobe and sidelobe signals, along with ensuring the compatibility of multiple constellations, can significantly enhance GNSS availability [49]. Table 1 shows the signal frequency, bandwidth, and modulation method information of GPS, Galileo, and BDS. It can be seen that the modulation methods of signals on the same frequency are different, resulting in signals that exhibit different characteristics in terms of tracking, interference, and multipath rejection performance.

After completing the estimation of multi-frequency and multi-constellation DCB, it is essential to conduct precision assessments of the obtained DCB products. Currently, the accuracy evaluation of DCB products focuses mainly on both internal and external conformity precision.

Table 1. GPS/GLONASS/Galileo/BDS signals.

Sys	Signal	Frequency	Bandwidth	Modulation
GPS	L1 C/A			BPSK (1)
	L1C	1575.42	30.69	BOC (1, 1) + TMBOC (6, 1, 4/33)
	L1P			BPSK (10)
	L1M			BOC (10, 5)
	L2C			BPSK (1)
	L2P	1227.6	30.69	BPSK (10)
	L2M			BOC (10, 5)
	L5	1176.45	24	QPSK (10)
GLONASS	L1OF	$1602 + k \times 0.5625$		FDMA and BPSK
	L2OF	$1246 + k \times 0.4375$	0.511	FDMA and BPSK
Galileo	E1	1575.42	24.552	MBOC (6, 1, 1/11)
	E5	1191.795	51.15	AltBOC (15, 10)
	E5a	1176.45	20.46	AltBOC (15, 10)
	E5b	1207.14	20.46	AltBOC (15, 10)
	E6	1278.75	40.92	BPSK (5)
BDS	B1I	1561.098	4.092	BPSK (2)
	B1C	1575.42	32.736	Data BOC (1, 1) Pilot QMBOC (6, 1, 4/33)
	B2a	1176.45	20.46	Data BPSK (10) Pilot BPSK (10)
	B2b	1207.14	20.46	BPSK (10)
	B3I	1268.520	20.46	BPSK (10)

Internal conformity precision primarily pertains to the stability of DCB. Since DCB is typically estimated as a daily value, the accuracy of DCB is assessed using stability indicators between consecutive days of the DCB sequence. The specific calculation formula is as follows:

$$S^i = \sqrt{\frac{\sum_{n=1}^{N}\left(DCB^i(n) - \overline{DCB^i}\right)}{N - 1}} \tag{8}$$

where S^i represents the stability indicator of the DCB sequence for the $i-th$ satellite, N is the total number of days in the DCB sequence, $DCB^i(n)$ denotes the DCB of the $i-th$ satellite on the $n-th$ day, and $\overline{DCB^i}$ represents the average value of the $i-th$ DCB.

In this paper, BDS-3 underwent an upgrade before September and October 2022, resulting in a discontinuity in the satellite DCB. Consequently, for statistical analysis, the time series of DCB is divided into two groups: before and after the upgrade. The formula for calculating the overall stability of the DCB sequence after the upgrade is as follows [50]:

$$\sqrt{\frac{(N_1 - 1)s_1{}^2 + (N_2 - 1)s_2{}^2 + \dfrac{N_1 N_2}{(N_1 + N_2)}(M_1^2 + M_2^2 - 2M_1 M_2)}{(N_1 + N_2 - 1)}} \tag{9}$$

where N_1 and N_2 represent the sample sizes of Group 1 and Group 2, respectively; M_1 and M_2 denote the mean values of Group 1 and Group 2, respectively; S_1 and S_2 indicate the standard deviations of Group 1 and Group 2, respectively.

The main verification method for external consistency accuracy is to compare the results with the DCB products published by IGS. When comparing products from different institutions, it is essential to address the issue of reference standardization first. Subsequently, statistical measures such as mean deviation and standard deviation are computed for the comparison.

2.4. Converting DCB to OSB

While converting DCB to OSB, we should choose the datum frequencies that are the same as the frequencies of clock offset products and the value of the OSB ionosphere-free

combination shall be guaranteed to be zero. The datum observation types selected in this paper are C2I and C6I.

Assuming n types of observations, there are $n-1$ DCB types relative to the reference after determining the reference observation types. Then, the remaining $n-1$ DCB types would be converted to OSB under the restrictive condition that the sum of the two observations in the ionosphere-free combination is zero. The conversion relationship between DCB and OSB is expressed as follows:

$$
\begin{bmatrix} DCB_{ij} \\ DCB_{ik} \\ \vdots \\ DCB_{in} \\ 0 \end{bmatrix} = \begin{bmatrix} 1 & -1 & \dots & 0 \\ 1 & 0 & \dots & 0 \\ \vdots & \vdots & & \vdots \\ 1 & 0 & \dots & -1 \\ \alpha_{ij} & \beta_{ij} & \dots & 0 \end{bmatrix} \begin{bmatrix} B_i \\ B_j \\ \vdots \\ B_n \end{bmatrix} \tag{10}
$$

where B_n is the pseudorange OSB corresponding to observation n; α_{ij} and β_{ij} are the ionosphere-free combination coefficient. After the derivation of the above equation, each observation type pseudorange OSB can be estimated.

$$
\begin{cases} \alpha_{ij} = \frac{f_i^2}{f_i^2 - f_j^2} \\ \beta_{ij} = \frac{f_j^2}{f_i^2 - f_j^2} \\ B_i = \beta_{ij} DCB_{ij} \\ B_j = -\alpha_{ij} DCB_{ij} \\ B_n = \beta_{ij} DCB_{ij} - DCB_{in} \end{cases} \tag{11}
$$

However, the OSB estimated from this algorithm only provides a bias that can be directly corrected from the raw observations which is not the real hardware delay but still essentially a combination of pseudorange hardware delays in the DCB form.

3. Estimation of Satellite DCB

3.1. Experimental Data

With the application of multi-frequency and multi-system receivers, we select 364 stations' observations from Day of year (Doy) 1, 2021 to 2023, Doy 213 for the experiment. The global distribution of stations selected for this experiment is depicted in Figure 1, with 364 stations capable of GPS signal tracking, 358 stations for GLONASS, 338 stations for Galileo, and 237 stations for BDS.
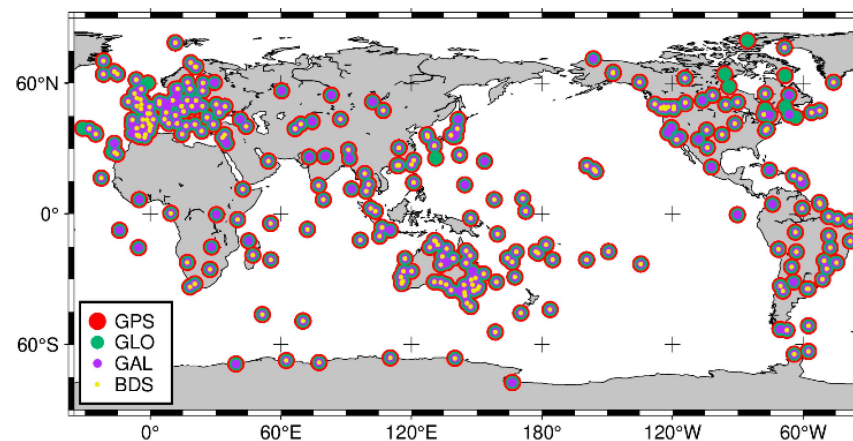

Figure 1. Distribution of multi-frequency and multi-system measurement stations (GPS: red, GLONASS: green, Galileo: purple, BDS: yellow).

3.2. BDS Satellite DCB Estimation Results

The current BDS constellation partly in normal operation state includes BDS-2 and BDS-3. The satellites of BDS-2 can only broadcast B1/B2/B3 signals with fewer types of DCBs, while BDS-3 adds new signals (B1C/B2a/B2b/B2 (a + b)); thus, the types of DCBs are significantly increased. Table 2 shows the types of DCB estimated in this paper. It is worth noting that although some studies regard BDS-2 and BDS-3 as two different systems, the same signals B1I and B3I exist in both BDS-2 and BDS-3; therefore, we take these two generations of BDS as the same system for estimating C2I-C6I DCB in this study. Moreover, as indicated in Table 2, we have exclusively estimated the DCB results for the C2I-C6I signal in the case of satellites C59 to C60, without extending the estimation to other types of DCB. In fact, satellites C59 and C60 can also transmit additional signals (B1C/B2a/B2b). However, information from the China Satellite Navigation System Management Office Test and Assessment Research Center website (https://www.csno-tarc.cn/system/constellation, accessed on 1 November 2024) indicates that these specific satellites primarily emit fundamental navigation signals such as B1I/B3I. Other signals serve predominantly for PPP services and the Satellite-Based Augmentation System (SBAS). Consequently, our analysis focuses exclusively on estimating the basic navigation signals of satellites C59 and C60.

**Table 2.** Estimated BDS DCB types.

Constellation	Satellite PRN	DCB Type
BDS-2	C01~C14, C16	C2I–C7I C2I–C6I
BDS-3	C19~C30, C32~C46, C59~C61	C2I–C6I
	C19~C30, C32~C46	C1P–C5P, C1X–C5X, C2I–C1P, C2I–C1X, C2I–C5P, C2I–C5X, C2I–C7Z, C2I–C8X, C5X–C7Z, C5X–C8X

Firstly, we estimated the DCB types related to the B1I signal, as presented in Table 2, with the results depicted in Figure 2. The figure illustrates that the DCB values for the majority of satellites exhibit a broad range. Specifically, the values for C2I–C5P, C2I–C5X, C2I–C7Z, and C2I–C8X fall within −80 to 30 ns. The C2I–C6I values range between −50 and 50 ns, while C2I–C7I ranges from −20 to 10 ns. The narrowest value range is observed for C2I–C1P and C2I–C1X, ranging from −5 to 5 ns. DCB types with broader ranges indicate greater variability and, thus, lower stability. The DCB values and trend directions between different channels for the same signals are similar. For instance, B1I and B1C (C2I–C1P, C2I–C1X), as well as B1I and B2 signals (C2I–C5P, C2I–C5X), exhibit similar patterns. Additionally, most satellites exhibit distinct yet comparable long-term trend changes, with synchronous jumps at identical time points.

Figure 2 illustrates notable jumps in the DCB of satellites C2I–C6I, C2I-C5P, C2I–C5X, C2I–C7Z, and C2I–C8X from September to October 2023. Nevertheless, there were no satellite replacements or additions during this period that could have resulted in alterations to satellite benchmarks. The Test and Assessment Research Center of the China Satellite Navigation Issued a notice on 14 June 2022, announcing a phased on-orbit software upgrade for the BDS-3 satellites. Throughout 2022, a total of 27 BDS System User Notices (NOTICE ADVISORY TO BDS USERS, NABU), numbered from 20220001 to 20220027, were released. These notices addressed the upgrade and maintenance of 27 BDS-3 satellites, including C19 through C27, C29 through C30, C32 through C37, C39 through C46, and C60 through C61. Following these notices, another notice (NO. 20220028) was issued regarding software and hardware maintenance for PRN 35, and a subsequent notice (NO. 20220029) detailed the precise schedule for hardware maintenance in the following month. Announcements related to in-orbit maintenance and operational summaries were also disseminated, with specific details available in the notice list (https://www.csno-tarc.cn/notice/index, ac-

cessed on 1 November 2024). The absence of distinctive characteristics in the DCB of the PRN35 satellite suggests that the correlation between the satellite DCB and parameters, such as the satellite orbital attitude, is not significant.

Considering that some types of DCB have experienced overall jumps, we used Equation (9) to statistically analyze their overall stability, as illustrated in Figure 3. After comparing the stability of these DCBs, we found that the DCBs between the B1I and B1C signals exhibit the highest stability, consistently remaining within a 0.5 ns range. In contrast, the stability of other DCB types is relatively weaker. This difference in stability is partly due to the fact that all DCBs, except those of B1I and B1C, experienced significant jumps during the BDS upgrade and maintenance period, which negatively impacted their stability. Additionally, the B1C signal benefits from superior signal strength and accuracy, contributing to its enhanced stability [51]. We then examine the DCBs of B1I and B2I signals in BDS-2, where the stability across all satellites ranges from 0.32 to 0.75, and their mean values generally remain within a 0.5 ns threshold. BDS-2 demonstrates superior stability, with most DCBs staying within a 1 ns range. In contrast, BDS-3 exhibits an average STD (standard deviation) of 1.77 ns, excluding satellites C45 and C46, whose stability reaches approximately 20 ns. This divergence is primarily attributed to upgrades in BDS-3 satellites. Although both BDS-2 and BDS-3 use the B1I and B3I signals, different receivers apply varying signal processing strategies, resulting in a time delay bias between BDS-2 and BDS-3 [52]. During DCB estimation, much of this delay bias is incorporated into the DCB, leading to increased estimation errors for BDS-3.
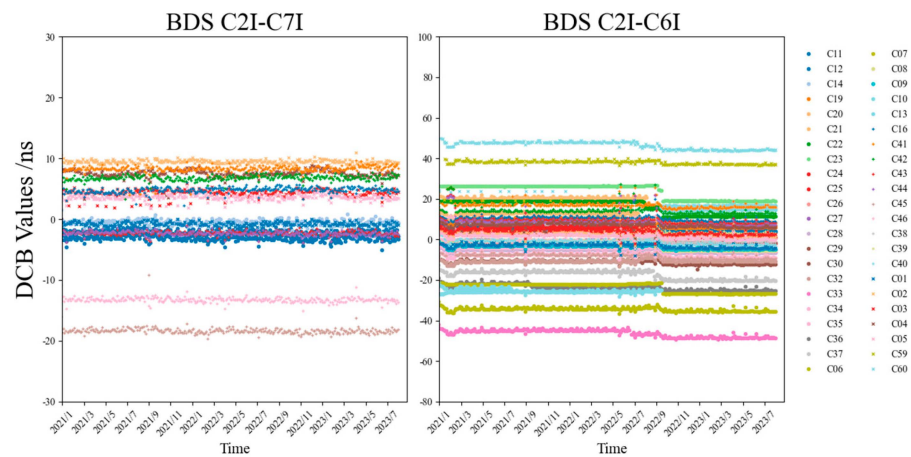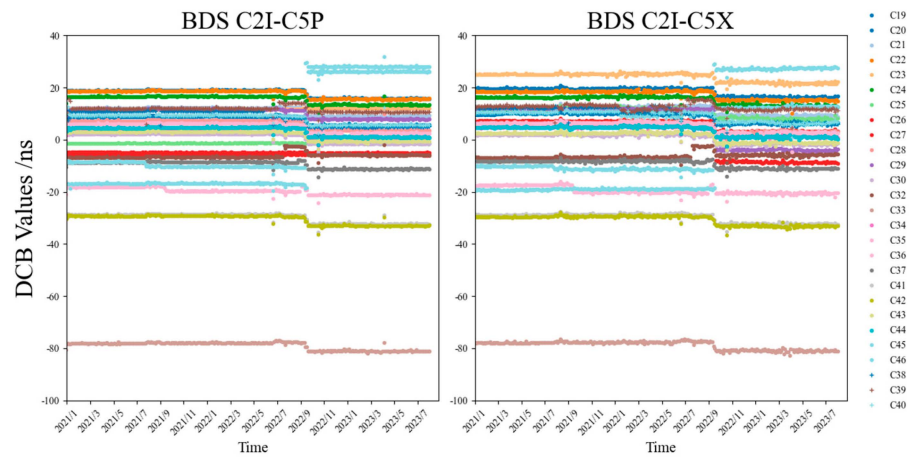

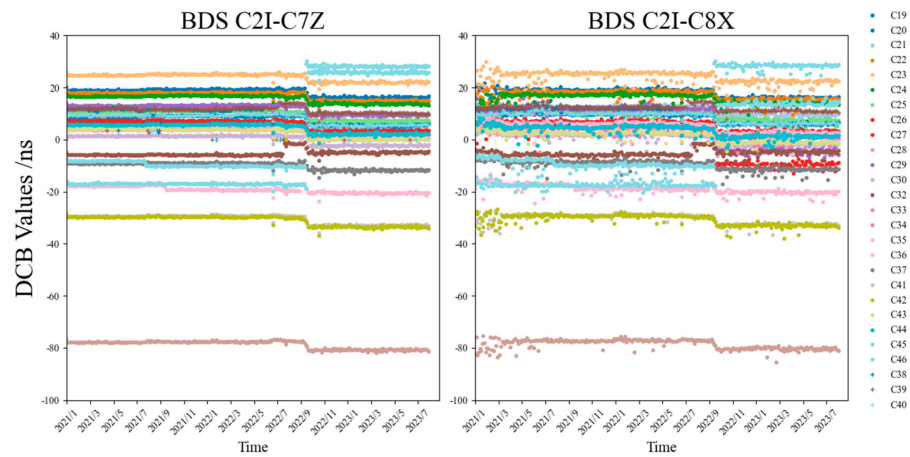(**a**) DCB of BDS B1 and B2 (left), B3 (right) signals
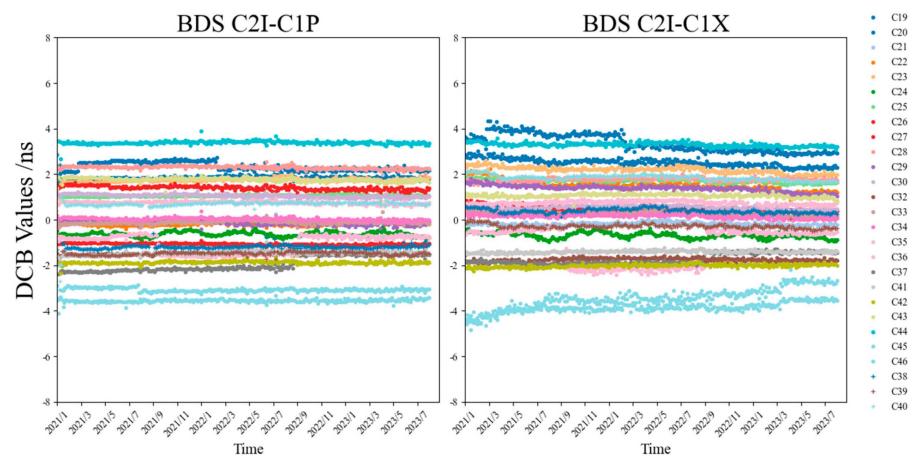
(**b**) DCB of BDS B1 and B1C signals

Figure 2. *Cont.*

BDS C2I-C5P

BDS C2I-C5X

(**c**) DCB of BDS B1 and B2a signals

BDS C2I-C7Z

BDS C2I-C8X

(**d**) DCB of BDS B1 and B2b, B2 (a + b) signals

Figure 2. BDS DCB time series between B1I signal and B2I, B3I, B1C, B2a, B2b, and B2 (a + b) signals from January 2021 to August 2023 for BDS.

BDS SDCB STD (ns)

	C19	C20	C21	C22	C23	C24	C25	C26	C27	C28	C29	C30	C32	C33	C34	C35	C36	C37	C38	C39	C40	C41	C42	C43	C44	C45	C46
C1P-C5P	1.472	1.49	1.534	1.527	1.843	1.52	0.09566	0.1206	0.134	1.714	1.697	1.707	1.098	1.487	1.759	1.677	1.309	1.586	2.773	1.094	1.804	1.781	1.8	1.724	1.711	20.31	17.93
C1X-C5X	1.611	1.507	1.614	1.609	1.495	1.508	1.73	7.285	1.744	1.731	7.328	1.744	1.092	1.516	1.732	1.82	1.512	1.608	2.877	1.234	1.896	1.768	1.811	1.748	1.772	14.61	18.01
C2I-C1P	0.3926	0.07017	0.07932	0.07538	0.08782	0.1066	0.04314	0.04314	0.09233	0.07587	0.0911	0.08037	0.07072	0.08634	0.06612	0.06739	0.5956	0.3267	0.2746	0.07641	0.2467	0.1003	0.0626	0.1145	0.07999	0.06779	0.09738
C2I-C1X	0.4254	0.1694	0.06956	0.2388	0.143	0.1319	0.08333	0.1077	0.07543	0.08108	0.1457	0.07632	0.07182	0.07575	0.08091	0.08925	0.8017	0.2423	0.09934	0.09158	0.1284	0.0544	0.06955	0.07491	0.08947	0.4699	0.2123
C2I-C5P	1.572	1.492	1.563	1.51	0.2235	1.518	0.0963	0.1386	0.1505	1.755	1.749	1.76	1.111	1.493	1.796	1.714	1.236	1.298	2.774	1.094	1.817	1.755	1.807	1.735	1.722	20.33	17.93
C2I-C5X	1.835	1.63	1.656	1.701	1.634	1.573	1.819	7.401	1.784	1.771	7.479	1.796	1.096	1.587	1.821	1.913	1.623	1.424	2.746	1.316	1.926	1.78	1.803	1.814	1.867	14.87	18.09
C2I-C7Z	1.603	1.461	1.673	1.49	1.449	1.921	1.7	1.764	1.818	1.777	1.727	1.791	1.124	6.458	1.685	1.847	1.936	1.444	3.191	2.023	2.199	1.742	2.53	1.796	1.778	20.2	17.88
C2I-C8X	1.98	1.748	1.899	1.939	2.043	1.952	2.325	7.377	2.056	2.131	7.421	2.25	1.391	1.809	2.202	2.142	1.866	1.814	2.862	1.288	1.939	1.954	2.058	1.944	2.189	14.66	17.9

Figure 3. The overall stability of BDS B1I signal and B2I, B3I, B1C, B2a, B2b, and B2 (a + b) signals.

We conducted a statistical analysis of the results based on the type of atomic clocks used (excluding satellites C45 and C46), as is shown in Table 3. We found that for DCBs of B1I signals compared to B2a, B2b, and B2 (a + b) signals, satellites equipped with Rubidium atomic clock exhibited higher stability than those with the hydrogen atomic clock. Conversely, for B1I and B1C signals, hydrogen atomic clocks demonstrated greater

stability than rubidium atomic clocks. This difference is primarily attributed to the B1C signal using the MBOC (6, 1, 1/11) modulation scheme, which facilitates compatibility and interoperability with GPS L1C and Galileo E1 OS signals, resulting in higher stability [51].

Table 3. Stability of DCB in different satellite clocks.

Clock Type	PRN	DCB Type	Mean STD
Rubidium atomic clock	C19, C20, C21, C22, C23, C24, C32, C33, C36, C37, C41, C42	C2I–C1P	0.132
		C2I–C1X	0.204
		C2I–C5P	1.341
		C2I–C5X	1.474
		C2I–C7Z	1.378
		C2I–C8X	1.799
hydrogen atomic clock	C25, C26, C27, C28, C29, C30, C34, C35, C38, C39, C40, C43, C44	C2I–C1P	0.102
		C2I–C1X	0.092
		C2I–C5P	1.415
		C2I–C5X	2.642
		C2I–C7Z	1.784
		C2I–C8X	2.865

3.3. DCB Compatibility Analysis

Since BDS and Galileo were developed later, frequency resources are extremely limited, necessitating negotiations for a common frequency resource by multiple parties. From the initial design and construction phase of the BDS-3 satellites, compatibility with other systems was a primary consideration. As compatible and interoperable technology advances, receivers can receive signals at the same frequency from multiple systems, thereby reducing the design cost of application terminals and enhancing the overall competitiveness of the satellite navigation industry. The types of DCBs for BDS, Galileo, and GPS with the same frequency are shown in Table 4. Although the satellite signal frequencies overlap and the signal waveforms are similar, the modulation methods differ. Therefore, in this paper, we analyze and verify the BDS compatible interoperability between DCBs with the same frequency to confirm the signal design performance.

Table 4. Code types for the same frequency.

Signal Frequency	Constellation	Code Type
1575.42 MHz	BDS	C1X, C1P
	Galileo	C1Q, C1X
	GPS	C1C, C1W
1176.45 MHz	BDS	C5X, C5P
	Galileo	C5Q, C5X
	GPS	C1Q, C5X

We estimated the DCB among compatible signals, and the results are depicted in Figure 4. Similar to the DCB performance discussed in the preceding section, the numerical ranges of DCBs for signals from various channels within the same constellation are close, showing analogous long-term trend changes. Among these, GPS satellite DCB values exhibit the smallest numerical range, primarily from −7 to 9 ns. Following that, the Galileo satellite DCB ranges from −7 to 12 ns, whereas BDS values range from −80 to 35 ns. Analyzing the time series results, the E1 and E5a signals, fundamental navigation signals for Galileo, exhibit greater stability, whereas there is an overall increasing trend in the satellite DCB values for GPS. In mid-September 2022, a notable jump occurred in the DCB of BDS B1C and B2a signals. The reason, similar to other DCBs in BDS, is due to the BDS-3 satellites upgrade maintenance.
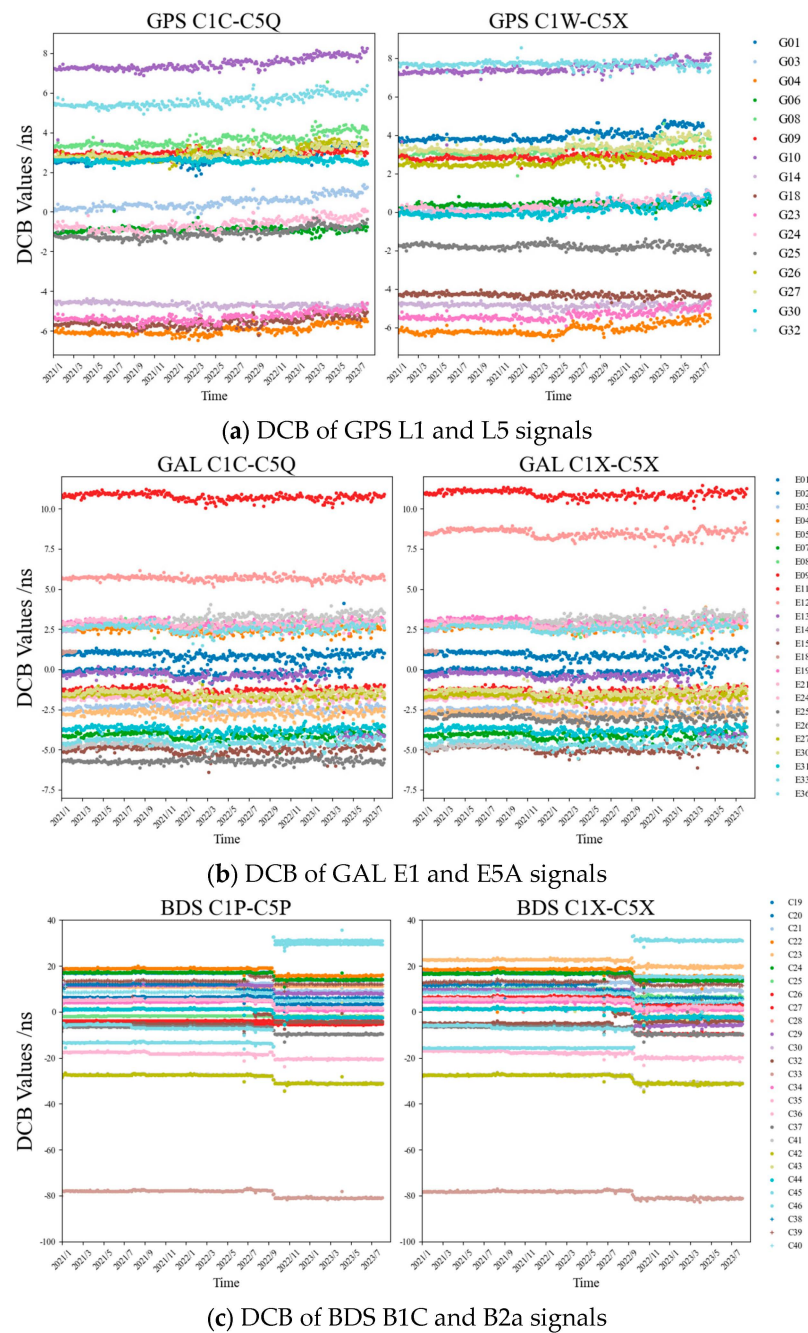
(**a**) DCB of GPS L1 and L5 signals

(**b**) DCB of GAL E1 and E5A signals

(**c**) DCB of BDS B1C and B2a signals

Figure 4. Time series of GPS/Galileo/BDS in January 2021 to August 2023, where (**a**) GPS DCB; (**b**) Galileo DCB; (**c**) BDS DCB.

We estimated the stability of DCB among compatible signals from the three satellite systems, as illustrated in Figure 5. BDS shows significantly lower stability compared to the other two systems. Except for satellites C45 and C46, most BDS satellite DCBs have stability within 2 ns. The IGSO satellite C38 exhibits poor stability, primarily due to lower-quality observational data. For GPS and Galileo, most satellites have stability around 0.4 ns. Specifically, the DCB stability of satellite E26 is poor, mainly due to an observed jump in 2021. Similarly to BDS, an official announcement regarding a planned maneuver was issued, resulting in a change in Galileo DCB from approximately −4 ns to 3 ns. For more detailed information, please refer to the official announcement on the NABU Information website.
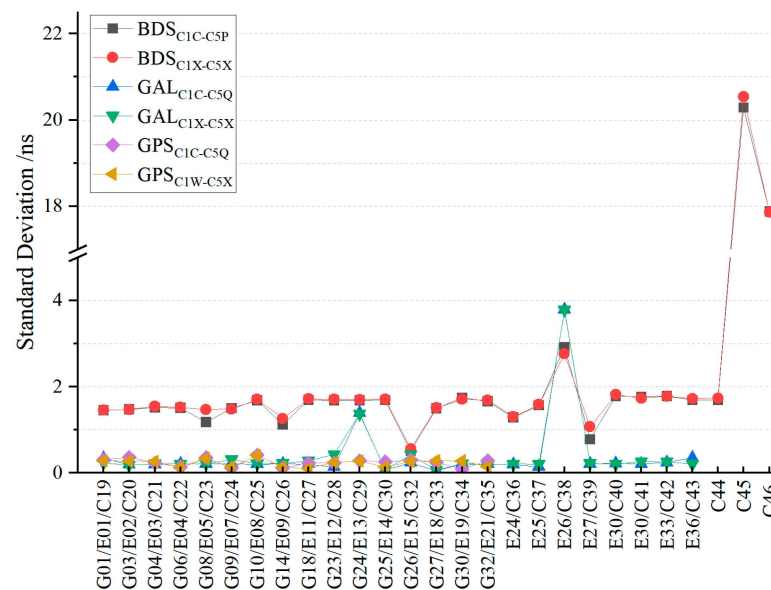
Figure 5. GPS/Galileo/BDS DCB mean STD in January 2021 to August 2023.

4. Estimation of Receiver DCB

In this section, we select multiple frequencies and multiple system receivers for analysis, and the number of stations is more than 10. Thus, six types of receivers are selected as shown in Table 5. Among them, SEPT POLARX5 receivers have the highest number of 82. Additionally, in this paper, most types of receivers can only receive one of the signal channels, either Q or X, from Galileo, and one of the signal channels, either P or X, from BDS.

Table 5. DCB types for the same frequency unit: ns.

Receiver Type	Stations Number	Observation Type
JAVAD TRE_3 DELTA	20	G: C1C C1W C1X C2W C2X C5X E: C1X C5X C6X C7X C8X C: C1X C2I C5X C6I C7I C7Z C8X
JAVAD TRE_G3TH_DELTA	13	G: C1C C1W C1X C2W C2X C5X E: C1X C5X C7X C: C2I C7I C7Z
LEICA GR50	18	G: C1C C1L C1W C2L C2W C5Q E: C1C C5Q C6C C7Q C8Q C: C1P C2I C5P C6I C7D C7I
SEPT POLARX5	82	G: C1C C1L C1W C2L C2W C5Q E: C1C C5Q C6C C7Q C8Q C: C1P C2I C5P C6I C7D C7I
SEPT POLARX5TR	22	G: C1C C2S C2W C5Q E: C1C C5Q C6C C7Q C8Q C: C1P C2I C5P C6I C7I
TRIMBLE ALLOY	40	G: C1C C1X C2W C2X C5X E: C1X C5X C6X C7X C8X C: C1X C2I C5X C6I C7D C7I

We conducted a statistical analysis on these receivers capable of receiving compatible signals, with the results presented in Figures 6–11. In comparison to satellite DCB, receiver DCB is similarly affected by hardware upgrades. For example, the DCB results for GPS and Galileo at the AJAC station showed a significant change around 2022, primarily due to a firmware upgrade on 15 December 2021, from LEICA GR50-4.51 to LEICA GR50-4.80. Although satellite DCB and receiver DCB are theoretically independent, in practical

GNSS data processing, receiver DCB is still influenced by residuals such as the ionosphere and satellite DCB. As demonstrated in Figures 6 and 7, nearly all receiver DCBs for BDS exhibited a significant change in November 2022.

We conducted a statistical analysis on the stability of DCB for GPS, Galileo, and BDS compatible signals based on receiver type, and the results are shown in the Table 6 below. Among the same type of receivers, Galileo receiver DCB has the best stability, followed by GPS, with BDS having the poorest stability. On one hand, the receiver DCB is affected by the residuals of the satellite DCB, resulting in decreased stability. On the other hand, it may be due to differences in the design of receivers by manufacturers, who consider variations in signal bandwidth, power spectral density, and other aspects among GPS, Galileo, and BDS. Consequently, the receiver's RF front end, responsible for down-converting and filtering the received satellite signals, may differ.

Furthermore, different receivers exhibit variations in receiving and processing GNSS signals: the number of satellite signal channels and the method of automatically allocating these channels can lead to differences in satellite signal timing within the receiver. In terms of signal processing, many modern receivers have started integrating multipath correction algorithms, such as SEPT A Posteriori Multipath Estimator (APME), or mechanisms for detecting and suppressing GNSS RF interference, which also affect the stability of the DCB.
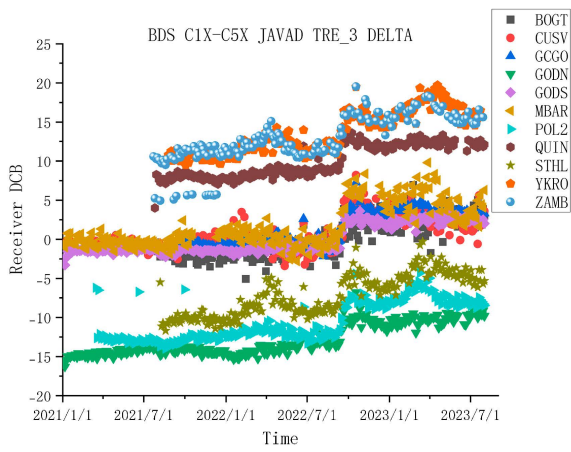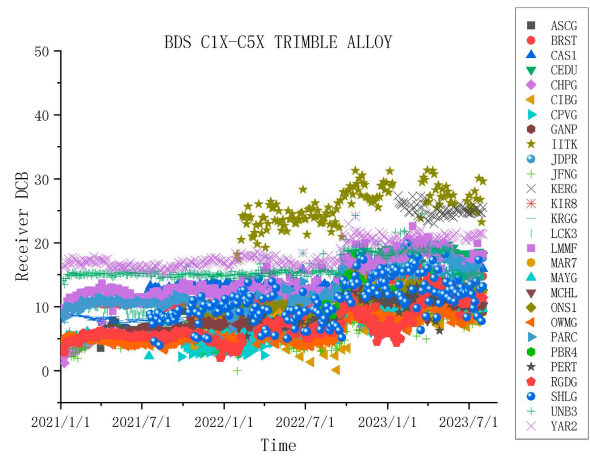

(**a**) LEICA GR50

(**b**) SEPT POLARX5
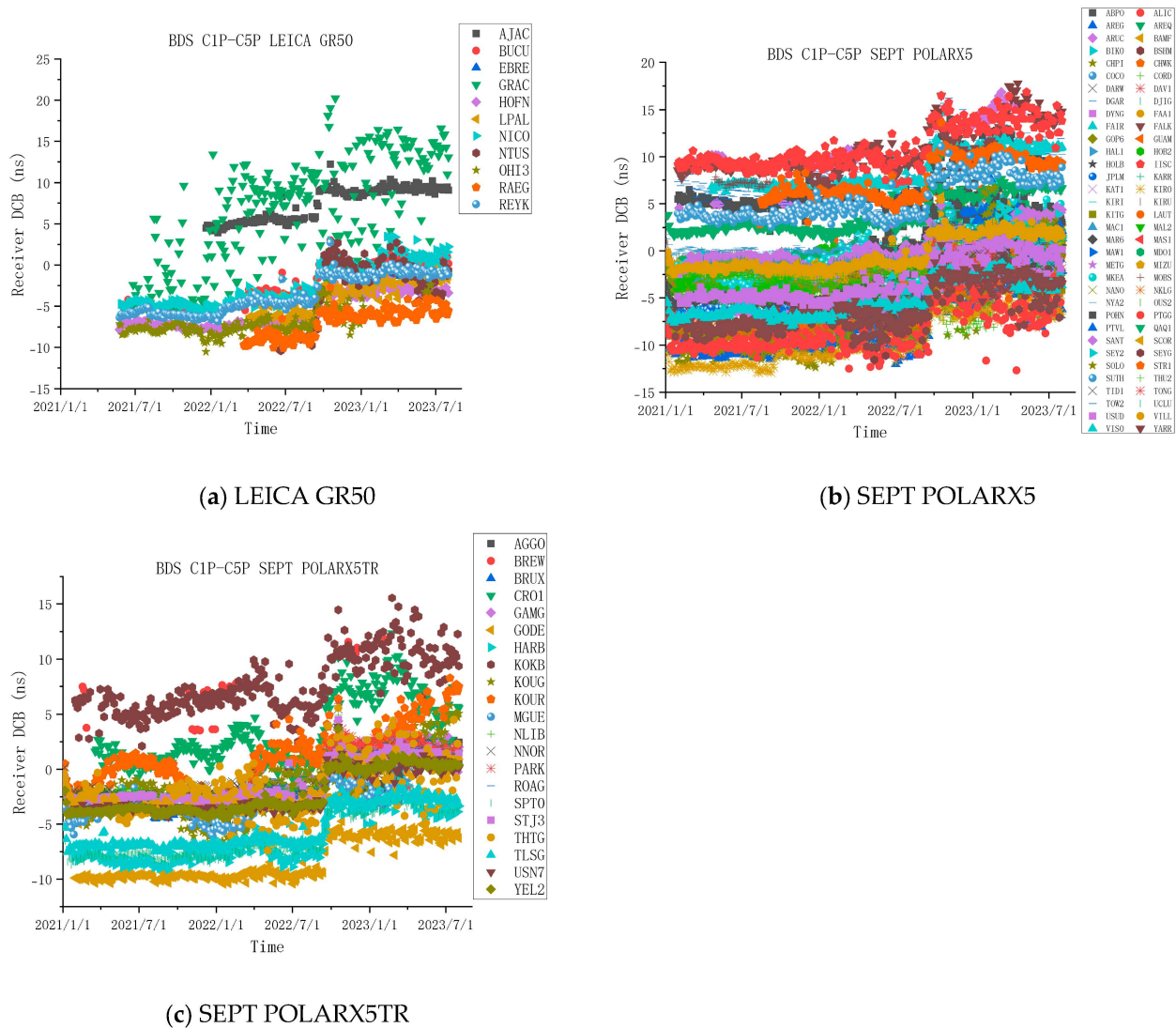
(**c**) SEPT POLARX5TR

Figure 6. BDS C1P–C5P receiver DCB time series.
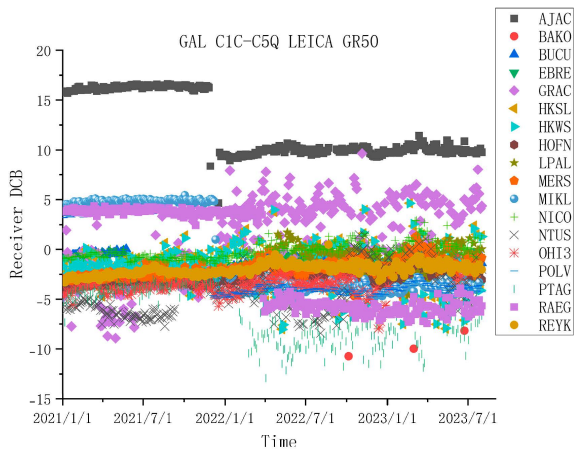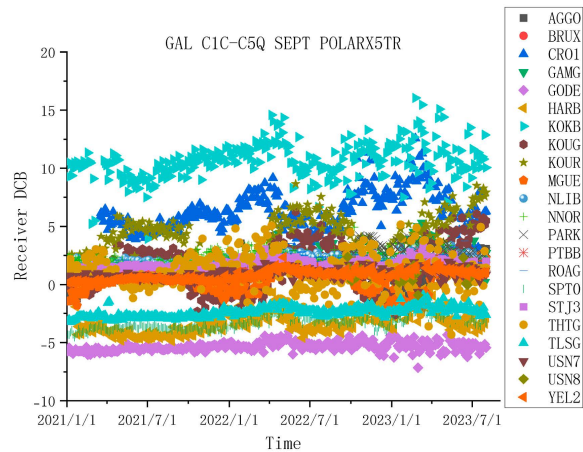
(**a**) JAVAD TRE_3 DELTA
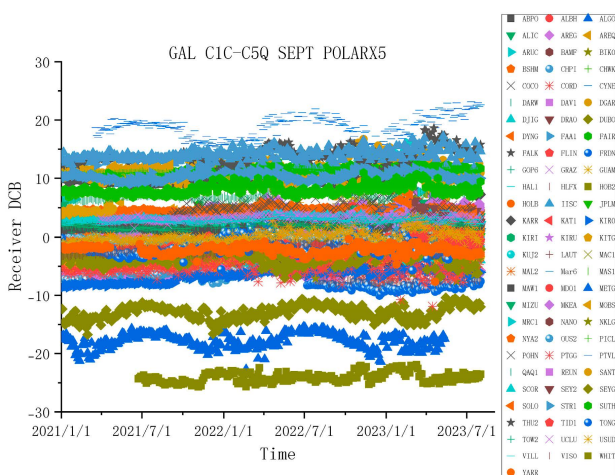
(**b**) TRIMBLE ALLOY

Figure 7. BDS C1X–C5X receiver DCB time series.

(**a**) LEICA GR50

(**b**) SEPT POLARX5TR

(**c**) SEPT POLARX5

Figure 8. GAL C1C–C5Q receiver DCB time series.

(**a**) JAVAD TRE_3 DELTA

(**b**) JAVAD TRE_G3TH DELTA
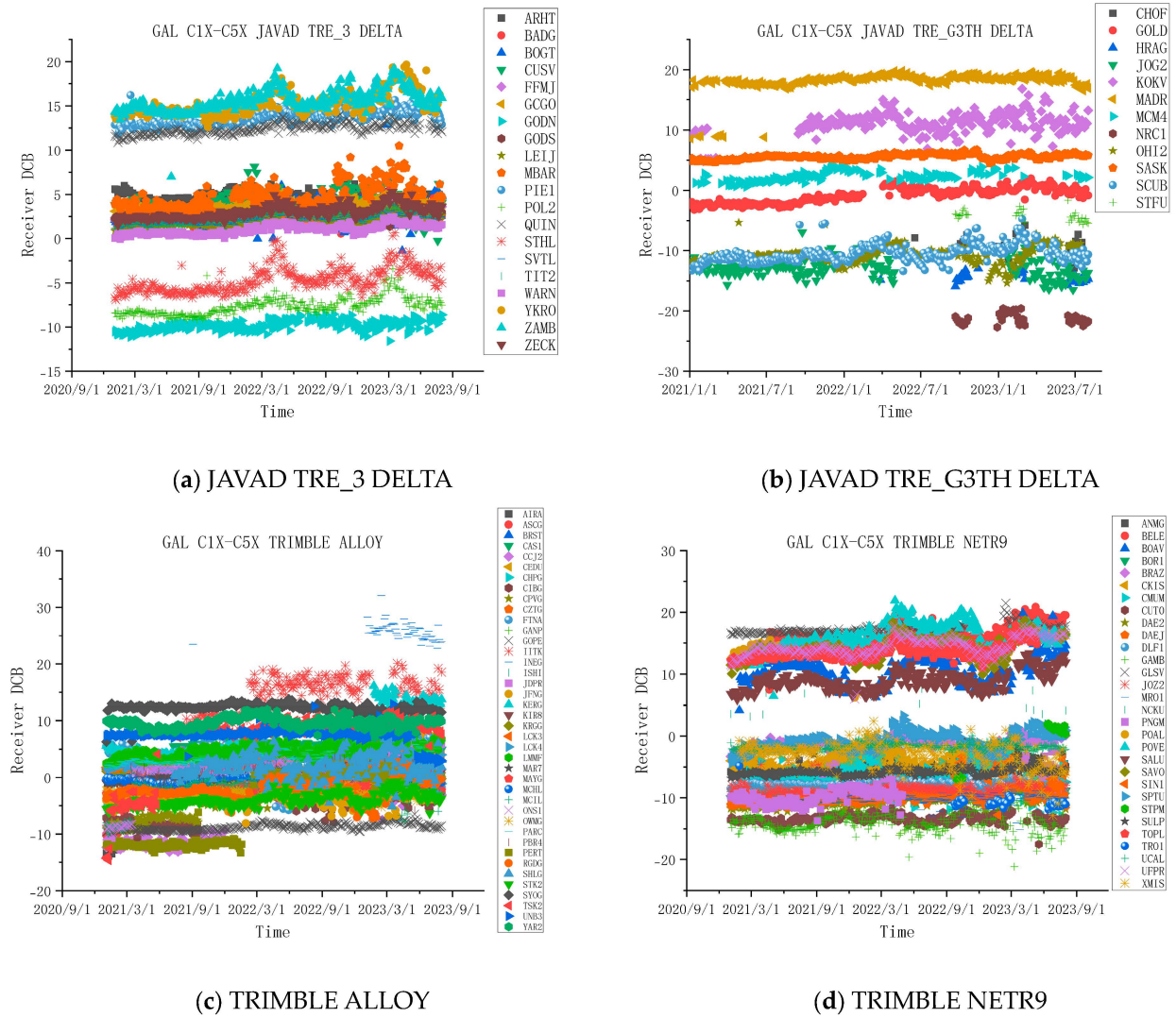

(**c**) TRIMBLE ALLOY

(**d**) TRIMBLE NETR9

Figure 9. GAL C1X–C5X receiver DCB time series.

Table 6. Compatibility signal DCB stability analysis.

Receiver Type	Sys	DCB Type	Mean STD (ns)
	BDS	C1P–C5P	3.128
LEICA GR50	GAL	C1C–C5Q	2.549
	GPS	C1C–C5Q	3.002
	BDS	C1P–C5P	2.339
SEPT POLARX5	GAL	C1C–C5Q	1.222
	GPS	C1C–C5Q	1.225
	BDS	C1P–C5P	2.203
SEPT POLARX5TR	GAL	C1C–C5Q	1.058
	GPS	C1C–C5Q	1.151
	BDS	C1X–C5X	2.370
JAVAD TRE_3 DELTA	GAL	C1X–C5X	0.906
	GPS	C1W–C5X	0.947
JAVAD TRE_G3TH DELTA	GAL	C1X–C5X	1.350
	GPS	C1W–C5X	1.421
TRIMBLE ALLOY	BDS	C1X–C5X	2.392
	GAL	C1X–C5X	2.195

(**a**) LEICA GR50

(**b**) SEPT POLARX5

(**c**) SEPT POLARX5TR

Figure 10. GPS C1C–C5Q receiver DCB time series.

(**a**) JAVAD TRE_3 DELTA

(**b**) JAVAD TRE_G3TH DELTA

Figure 11. GPS C1W–C5X receiver DCB time series.

5. DCB Consistency Analysis

5.1. Comparison Results with Other Institutions

In this subsection, we use CAS products to compare and evaluate the performance of our results. Since the types of satellite DCB published by CAS are generally different from those we use, we obtain equivalent DCB types through linear combinations. The DCB types published by CAS are listed in Table 7, and the combined DCB is represented by Equation (12):

$$
\begin{cases}
DCB_{C2I-C1P}^{CAS,BDS} = DCB_{C2I-C6I}^{CAS,BDS} - DCB_{C1P-C6I}^{CAS,BDS} \\
DCB_{C2I-C1X}^{CAS,BDS} = DCB_{C2I-C6I}^{CAS,BDS} - DCB_{C1X-C6I}^{CAS,BDS} \\
DCB_{C2I-C5P}^{CAS,BDS} = DCB_{C2I-C6I}^{CAS,BDS} - DCB_{C1P-C6I}^{CAS,BDS} + DCB_{C1P-C5P}^{CAS,BDS} \\
DCB_{C2I-C5X}^{CAS,BDS} = DCB_{C2I-C6I}^{CAS,BDS} - DCB_{C1X-C6I}^{CAS,BDS} + DCB_{C1X-C5X}^{CAS,BDS} \\
DCB_{C2I-C7Z}^{CAS,BDS} = DCB_{C2I-C6I}^{CAS,BDS} - DCB_{C1X-C6I}^{CAS,BDS} + DCB_{C1X-C7Z}^{CAS,BDS} \\
DCB_{C2I-C8X}^{CAS,BDS} = DCB_{C2I-C6I}^{CAS,BDS} - DCB_{C1X-C6I}^{CAS,BDS} + DCB_{C1X-C8X}^{CAS,BDS} \\
DCB_{C1W-C5X}^{CAS,BDS} = DCB_{C1C-C5X}^{CAS,BDS} - DCB_{C1C-C1W}^{CAS,BDS}
\end{cases}
\tag{12}
$$

Table 7. Validated DCB types.

Constellation	Code Type
BDS	C2I–C7I, C2I–C6I C1X–C5X, C1P–C5P C1X–C6I, C1P–C6I C1X–C7Z, C1X–C8X
GPS	C1C–C1W C1C–C5Q, C1C–C5X
Galileo	C1C–C5Q, C1C–C5X

We will compare our computed results with those provided by CAS, as is shown in Figure 12 and Table 8. We find that, compared to the combined DCBs, the directly estimated average deviations are generally smaller. Specifically, the average deviation and STD for the new BDS signals, B1C and B2a, are the smallest, typically below 0.2 ns. For the fundamental navigation signals of BDS, the DCB for BDS-3 shows significantly better average deviation and stability compared to BDS-2, usually remaining below 0.2 ns. Furthermore, C2I–C1P and C2I–C1X exhibit a minor average STD within 0.2 ns, with average deviations slightly higher but still generally below 0.8 ns. The average deviation and STD of C2I–C7Z and C2I–C8X are relatively larger, yet they remain stable within 1 ns. Comparing C2I–C1P, C2I–C5P, C2I–C1X, and C2I–C5X, we observe that the average deviations of DCBs for different satellites show similar trends in both P and X channels.

Table 8. BDS DCB mean STD.

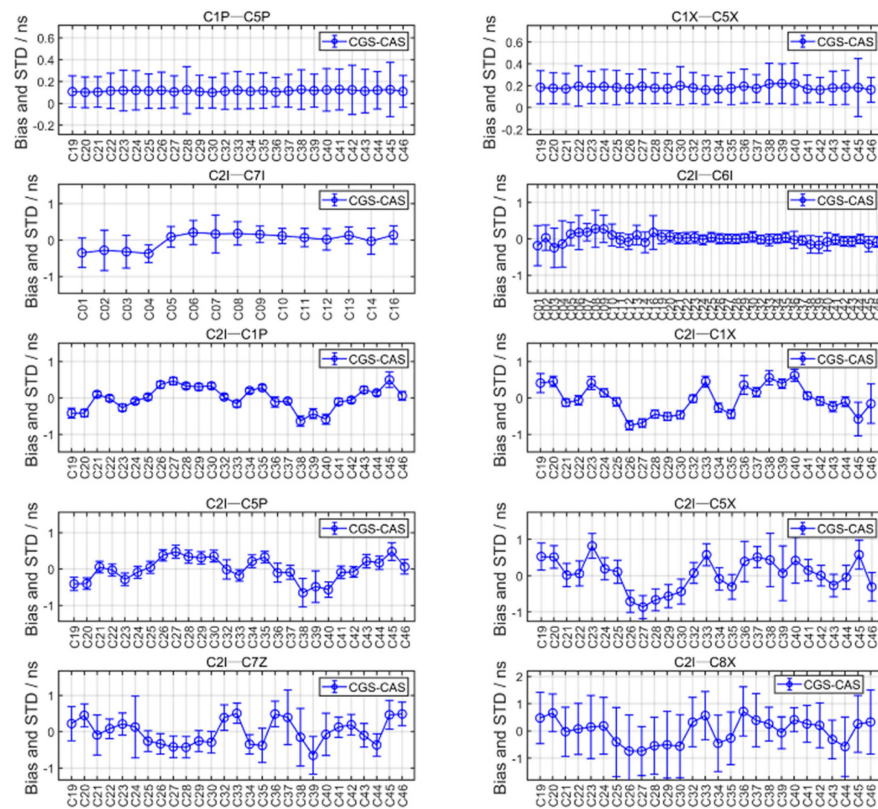| BDS DCB Type	Mean STD
C1P–C5P	0.177
C1X–C5X	0.153
C2I–C7I	0.328
C2I–C6I	0.236
C2I–C1P	0.098
C2I–C1X	0.166
C2I–C5P	0.200
C2I–C5X	0.374
C2I–C7Z	0.399
C2I–C8X	0.941

Figure 12. Comparison results of BDS DCB mean bias and STD.

Similarly, we conducted a comparative analysis of the average deviations and STD for GPS C1C–C5Q, C1W–C5X, and Galileo C1C–C5Q, C1X–C5X DCBs, as illustrated in Figure 13 and Table 9. It is evident that GPS C1C–C5Q and Galileo C1C–C5Q, C1X–C5X DCBs exhibit good consistency, with average deviations and standard deviations generally within the range of 0.2 ns. Although the average deviation for GPS C1W–C5X is relatively large, it remains generally stable within 0.6 ns, and the standard deviation is also typically within 0.2 ns.
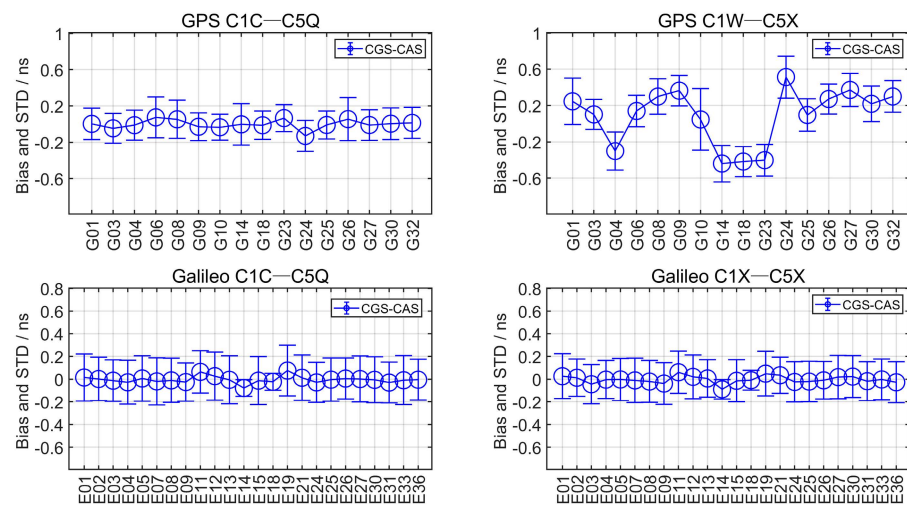
Figure 13. Comparison results of GPS and Galileo DCB mean bias and STD.

Table 9. GPS and Galileo DCB mean STD.

BDS DCB Type	Mean STD
GPS C1C–C5Q	0.186
GPS C1W–C5X	0.172
GAL C1C–C5Q	0.177
GAL C1X–C5X	0.198

5.2. Analysis of OSB Results

The DCB is defined as the difference in hardware delay deviation between two observations, and constraints can be added to convert the DCB with relative characteristics to an absolute bias of a single observation, i.e., the OSB. In this subsection, we convert the previously estimated DCB types, and the converted OSB includes nine types (C2I, C6I, C7I, C1P, C1X, C5P, C5X, C7Z, C8X). Among them, BDS has the most OSB types, whereas C7I is the observation code type broadcast only by BDS-2, and the other observation code types are broadcast by BDS-3.

Considering that we use OSB converted by the DCB method, the accuracy of the OSB also represents the accuracy of estimated DCB. Therefore, we count the RMS of the converted OSB, and the RMS statistics method is consistent with the law of propagation of errors from Equation (9).

Figure 14 presents the mean RMS of BDS OSBs, where most OSB types exhibit RMS values within 0.1 ns. Notably, the OSB RMS values for C5X and C7Z are particularly small, around 0.01 ns, reflecting the higher stability of these frequency signals. Comparing the reference frequencies of BDS, it is evident that the stability of C2I is superior to that of C6I, which is attributed to C2I being used as the reference frequency when converting to OSB. The RMS values for C1P and C1X OSB types are relatively larger than those for other OSB types, primarily due to the higher RMS values of C2I–C1P and C2I–C1X DCBs, which are generally around 1.2–1.3 ns. The increased RMS for these two DCB types can be attributed to the similarity in the observation frequencies. Table 10 shows the coefficients of the electronic content from Equation (3), revealing that the coefficients for these similar frequencies are smaller. This smaller coefficient significantly affects the observed values when estimating the DCB.
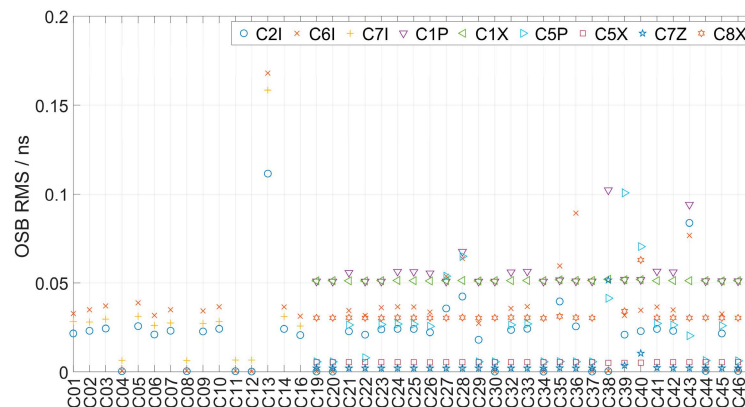

Figure 14. Mean RMS of BDS OSB.

Table 10. Coefficients before electron content.

	C1	C2	C5	C6	C7	C8
C1	0	−0.00299	−0.12881	−0.08807	−0.11419	−0.12136
C2	0.00299	0	−0.12581	−0.08508	−0.11119	−0.11836
C5	0.12881	0.12581	0	0.04073	0.01462	0.00745

Table 10. *Cont.*

	C1	C2	C5	C6	C7	C8
C6	0.08807	0.08508	−0.04073	0	−0.02612	−0.03328
C7	0.11419	0.11119	−0.01462	0.02612	0	−0.00717
C8	0.12136	0.11836	−0.00745	0.03328	0.00717	0

6. Conclusions

The experiment is based on observations from 364 stations that can track multi-constellation signals and are evenly distributed worldwide. In a multi-frequency and multi-constellation environment, global ionospheric maps are used as constraints to estimate the BDS-3/GNSS DCB. Furthermore, the DCB of the BDS/GPS/Galileo compatible signals is analyzed and evaluated, along with the receiver DCB. Then, an external conformity accuracy test is conducted using CAS multi-system DCB products. To further verify the DCB accuracy, the DCB is converted into OSB. The results of this study show the following:

(1) Between two signals of the same frequency but different channels, the numerical range and trend of DCB are similar. Satellite DCBs for C2I–C6I, C2I–C5P, C2I–C5X, C2I–C7Z, and C2I–C8X experienced significant jumps in September to October 2023, possibly due to China's official upgrade and maintenance of 30 BDS-3 satellites in orbit. Except for the C45 and C46 DCBs between B1I and B1C signals, which do not show significant jumps and exhibit relatively smooth stability, we speculate that there were no adjustments to the B1C signal during this upgrade.

(2) The stability of satellite DCBs equipped with rubidium clocks is better than those with hydrogen atomic clocks.

(3) For BDS/GPS/Galileo compatible signals (BDS B1C and B2a, GPS L1 and L5, Galileo E1 and E5A), the stability of BDS is noticeably weaker than the other two satellite systems.

(4) Among the same type of receivers, Galileo receiver DCB has the best stability, followed by GPS, with BDS having the poorest stability. This is primarily due to differences in the receiver's hardware design and the methods used for signal processing.

(5) The DCB estimated in this paper has high consistency with uncombined CAS products, while the mean bias and STD of most satellite DCBs are within 0.2 ns.

(6) In order to further verify the performance of DCB, we counted the OSB RMS and found that the OSB RMS of BDS C5Xand C7Z is smaller, and the RMS of C1P and C1X OSB is larger due to the small frequency difference between B1C and B1I signals, resulting in the observation equation being more affected by the quality of the observations.

References

1. Schaer, S. Mapping and Predicting the Earth's Ionosphere Using the Global Positioning System. Ph.D. Thesis, Astronomical Institute, University of Bern, Bern, Switzerland, 1999.
2. Dolin, S.V. Application of Differential Code Biases in Multi-GNSS Measurements in Real-Time Precise Point Positioning. *Gyroscopy Navig.* **2022**, *13*, 276–282. [CrossRef]
3. Sardon, E.; Rius, A.; Zarraoa, N. Estimation of the transmitter and receiver differential biases and the ionospheric total electron content from global positioning system observations. *Radio Sci.* **1994**, *29*, 577–586. [CrossRef]
4. Wilson, B.D.; Mannucci, A.J. Instrumental biases in ionospheric measurement derived from GPS data. In Proceedings of the 6th International Technical Meeting of the Satellite Division of The Institute of Navigation (ION GPS 1993), Salt Lake City, UT, USA, 22–24 September 1993; pp. 1343–1351.
5. Odolinski, R.; Teunissen, P.J.G. Low-cost, high-precision, single frequency GPS–BDS RTK positioning. *GPS Solut.* **2017**, *21*, 1315–1330. [CrossRef]
6. Long, T.; Zhang, X.; Xin, L.; Chen, Y. Estimation of Compass Satellite Differential Code Biases Using Combined GPS/Compass Observation. In Proceedings of the China Satellite Navigation Conference (CSNC 2012), Guanzhou, China, 15–19 May 2012; pp. 365–371.
7. Li, M.; Yuan, Y.; Zhang, X.; Zha, J. A multi-frequency and multi-GNSS method for the retrieval of the ionospheric TEC and intraday variability of receiver DCBs. *GPS Solut.* **2020**, *94*, 102. [CrossRef]
8. Klobuchar, J.A. Ionospheric time-delay algorithm for single-frequency GPS users. *IEEE Trans. Aerosp. Electron. Syst.* **1987**, *AES-23*, 325–331. [CrossRef]
9. Prieto-Cerdeira, R.; Orús-Pérez, R.; Breeuwer, E.; Lucas-Rodriguez, R.; Falcone, M. Performance of the Galileo single-frequency ionospheric correction during in-orbit validation. *GPS World* **2014**, *25*, 53–58.
10. Hong, C.K.; Grejner-Brzezinska, D.A.; Kwon, J.H. Efficient GPS receiver DCB estimation for ionosphere modeling using satellite-receiver geometry changes. *Earth Planets Space* **2008**, *60*, e25–e28. [CrossRef]
11. Ciraolo, L.; Azpiicueta, F.; Brunini, C.; Meza, A.; Radicella, S. Calibration errors on experimental slant total electron content (TEC) determined with GPS. *J. Geod.* **2007**, *81*, 111–120. [CrossRef]
12. Leandro, R.F.; Langley, R.B.; Santos, M.C. Estimation of P2-C2 Biases by Means of Precise Point Positioning. In Proceedings of the 63rd Annual Meeting of The Institute of Navigation, Cambridge, MA, USA, 23–25 April 2007; pp. 225–231.
13. Li, H.; Xu, T.; Huang, S.; Wang, J. A new differential code bias (C1-P1) estimation method and its performance evaluation. *GPS Solut.* **2016**, *20*, 321–329. [CrossRef]
14. Liu, T.; Zhang, B.; Yuan, Y.; Wang, N. Multi-GNSS triple-frequency differential code bias (DCB) determination with precise point positioning (PPP). *J. Geod.* **2019**, *93*, 765–784. [CrossRef]
15. Shi, C.; Fan, L.; Li, M. An enhanced algorithm to estimate BDS satellite's differential code biases. *J. Geod.* **2016**, *90*, 161–177. [CrossRef]
16. Fan, L.; Li, M.; Wang, C. BDS satellite's differential code biases estimation based on uncombined precise point positioning with triple-frequency observable. *Adv. Space Res.* **2017**, *59*, 804–814. [CrossRef]
17. Liu, A.; Li, Z.; Wang, N. Analysis of the short-term temporal variation of differential code bias in GNSS receiver. *Measurement* **2020**, *153*, 107448. [CrossRef]
18. Jin, S.; Wang, Q.; Dardanelli, G. A Review on Multi-GNSS for Earth Observation and Emerging Applications. *Remote Sens.* **2022**, *14*, 3930. [CrossRef]
19. Yasyukevich, Y.V.; Mylnikova, A.A.; Kunitsyn, V.E.; Padokhin, A.M. Influence of GPS/GLONASS differential code biases on the determination accuracy of the absolute total electron content in the ionosphere. *Geomagn. Aeron.* **2015**, *55*, 763–769. [CrossRef]
20. Mylnikova, A.A.; Yasyukevich, Y.V.; Kunitsyn, V.E. Variability of GPS/GLONASS differential code biases. *Results Phys.* **2015**, *5*, 9–10. [CrossRef]
21. Li, M.; Yuan, Y.; Wang, N.; Li, Z.; Li, Y.; Huo, X. Estimation and analysis of Galileo differential code biases. *J. Geod.* **2016**, *91*, 279–293. [CrossRef]
22. Montenbruck, O.; Hauschild, A.; Steigenberger, P. Differential code bias estimation using multi-GNSS observations and global ionosphere maps. *J. Inst. Navig.* **2014**, *61*, 191–201. [CrossRef]
23. Shi, Q.; Jin, S. Variation Characteristics of Multi-Channel Differential Code Biases from New BDS-3 Signal Observations. *Remote Sens.* **2022**, *14*, 594. [CrossRef]
24. Mi, X.; Sheng, C.; El-Mowafy, A.; Zhang, B. Characteristics of receiver-related biases between BDS-3 and BDS-2 for five frequencies including inter-system biases, differential code biases, and differential phase biases. *GPS Solut.* **2021**, *25*, 113. [CrossRef]
25. Zheng, F. Accounting for biases between BDS-3 and BDS-2 overlap B1I/B3I signals in BeiDou global ionospheric modeling and DCB determination. *Adv. Space Res.* **2022**, *69*, 3677–3691. [CrossRef]

26. Jin, S.; Jin, R.; Li, D. Assessment of BDS differential code bias variations from multi-GNSS network observations. *Ann. Geophys.* **2016**, *34*, 259–269. [CrossRef]

27. Wijaya, D.D.; Utama, A.K.; Kuntjoro, W. A two-step estimation of GPS differential code biases and local ionospheric TEC based on orthogonal transformation. *IEEE Trans. Geosci. Remote Sens.* **2023**, *61*, 5802214. [CrossRef]

28. Wang, Q.; Jin, S.; Ye, X. A Novel Method to Estimate Multi-GNSS Differential Code Bias without Using Ionospheric Function Model and Global Ionosphere Map. *Remote Sens.* **2022**, *14*, 2002. [CrossRef]

29. Wang, Q.; Zhu, J.; Feng, H. Ionosphere Total Electron Content Modeling and Multi-Type Differential Code Bias Estimation Using Multi-Mode and Multi-Frequency Global Navigation Satellite System Observations. *Remote Sens.* **2023**, *15*, 4607. [CrossRef]

30. Yuan, H.; Zhang, Z.; He, X. Stability Analysis of BDS-3 Satellite Differential Code Bias and Its Impacts on Single Point Positioning. *Geomat. Inf. Sci. Wuhan Univ.* **2023**, *48*, 425–432.

31. Liu, Y.; Zhang, Z.; OU, M. Long-term Variation of Differential Code Biases of Ionospheric TEC Monitor Based on Hardware Signal Simulator. *J. Space Sci.* **2021**, *41*, 499–504. [CrossRef]

32. Xiang, Y.; Xu, Z.; Gao, Y.; Yu, W. Understanding long-term variations in GPS differential code biases. *GPS Solut.* **2020**, *24*, 118. [CrossRef]

33. Bao, S.; Liu, H.; Xu, L.; Gong, X. Analysis of satellite-induced factors affecting the accuracy of the BDS satellite differential code bias. *GPS Solut.* **2017**, *21*, 905–916.

34. Cui, J.; Chen, J.; Wang, B.; Yu, C. Characteristic Analysis of Satellite DCB Products Provided by CAS and DLR. *Prog. Astron.* **2020**, *40*, 429–440.

35. Wang, Q.; Jin, S.; Hu, Y. Epoch-by-epoch estimation and analysis of BeiDou Navigation Satellite System (BDS) receiver differential code biases with the additional BDS-3 observations. *Ann. Geophys.* **2020**, *38*, 1115–1122. [CrossRef]

36. Gu, J.; Song, C.; Tian, K. Precision Single Point Positioning Accuracy Analysis of BDS-3 New Frequencies Based on OSB Correction. *Geod. Geodyn.* **2023**, *43*, 18–22.

37. Wang, N.; Li, Z.; Duan, B.; Hugentobler, U.; Wang, L. GPS and GLONASS observable-specific code bias estimation: Comparison of solutions from the IGS and MGEX networks. *J. Geod.* **2020**, *94*, 1–15. [CrossRef]

38. Deng, Y.; Guo, F.; Ren, X.; Ma, F.; Zhang, X. Estimation and analysis of multi-GNSS observable-specific code biases. *GPS Solut.* **2021**, *25*, 100. [CrossRef]

39. Montenbruck, O.; Peter, S.; Jean-Marie, S. Data+ pilot biases in modern GNSS signals. *GPS Solut.* **2023**, *27*, 112. [CrossRef]

40. Su, K.; Jiao, G. Estimation of BDS pseudorange biases with high temporal resolution: Feasibility, affecting factors, and necessity. *Satell. Navig.* **2023**, *4*, 17. [CrossRef]

41. Su, K.; Jiao, G. Two modified multi-frequency GNSS approaches to estimate the pseudorange observable-specific signal bias for the CDMA and FDMA models. *GPS Solut.* **2023**, *27*, 83. [CrossRef]

42. Ren, X.; Chen, J.; Li, X. Multi-GNSS contributions to differential code biases determination and regional ionospheric modeling in China. *Adv. Space Res.* **2020**, *65*, 221–234. [CrossRef]

43. Jin, R.; Jin, S.; Feng, G. M_DCB: Matlab code for estimating GNSS satellite and receiver differential code biases. *GPS Solut.* **2012**, *16*, 541–548. [CrossRef]

44. Brunini, C.; Azpilicueta, F. GPS slant total electron content accuracy using the single layer model under different geomagnetic regions and ionospheric conditions. *J. Geod.* **2010**, *84*, 293–304. [CrossRef]

45. Wang, Y.; Zhao, L.; Gao, Y. Estimation and Analysis of GNSS Differential Code Biases (DCBs) Using a Multi-Spacing Software Receiver. *Sensors* **2021**, *21*, 443. [CrossRef] [PubMed]

46. Januszewski, J. The Problem of Compatibility and Interoperability of Satellite Navigation Systems in Computation of User's Position. *Artif. Satell.* **2011**, *46*, 93–102. [CrossRef]

47. Sarkar, S. A study on compatibility and interoperability among multi-GNSS. *Aeronaut. Aerosp. Open Access J.* **2021**, *5*, 25–31. [CrossRef]

48. Sun, Y. Optimal parameter design of continuous phase modulation for future GNSS signals. *IEEE Access* **2021**, *9*, 58487–58502. [CrossRef]

49. Yang, J. Availability analysis of GNSS signals above GNSSs constellation. *J. Navig.* **2021**, *74*, 446–466. [CrossRef]

50. Altman, D.G.; Machin, D.; Bryant, T.N.; Gardner, M.J. *Statistics with Confidence*, 2nd ed.; BMJ Books: London, UK, 2000; pp. 28–31.

51. Zhang, Q.; Zhu, Y.; Chen, Z. An In-Depth Assessment of the New BDS-3 B1C and B2a Signals. *Remote Sens.* **2021**, *13*, 788. [CrossRef]

52. Jiao, G.; Song, S.; Jiao, W. Improving BDS-2 and BDS-3 joint precise point positioning with time delay bias estimation. *Meas. Sci. Technol.* **2019**, *31*, 025001. [CrossRef]